Quasi-2-day wave in low-latitude atmospheric winds as viewed from the ground and space during January-March, 2020

Maosheng He[1,1], Jorge L. Chau[1,1], Jeffrey M Forbes[2,2], Xiaoli Zhang[2,2], Christoph R Englert[3,3], Brian J Harding[4,4], Thomas J. Immel[5,5], Lourivaldo M. Lima[6,6], S. VijayaBhaskara Rao[7,7], Madineni Venkat Ratnam[8,8], Guozhu Li[9,9], John M Harlander[10,10], Kenneth D Marr[11,11], and Jonathan J. Makela[12,12]

[1]Leibniz-Institute of Atmospheric Physics at the Rostock University
[2]University of Colorado Boulder
[3]Naval Research Laboratory
[4]UC Berkeley
[5]University of California, Berkeley
[6]Universidade Estadual de Paraiba
[7]S.V. University
[8]National Atmospheric Research Laboratory
[9]Institute of Geology and Geophysics, Chinese Academy of Sciences
[10]St. Cloud State University
[11]Space Science Division, U.S. Naval Research Laboratory
[12]University of Illinois at Urbana Champaign

November 30, 2022

Abstract

Horizontal winds from four low-latitude (+/-15o) specular meteor radars (SMRs) and the MIGHTI instrument on the ICON satellite, are combined to investigate quasi-2-day waves (Q2DWs) in early 2020. SMRs cover 80-100 km altitude whereas MIGHTI covers 95-300 km. Q2DWs are the largest dynamical feature of the summertime middle atmosphere. At the overlapping altitudes, comparisons between the derived Q2DWs exhibit excellent agreement. The SMR sensor array analyses show that the dominant zonal wavenumbers are s=+2 and +3, and help resolve ambiguities in MIGHTI results. We present the first Q2DW depiction for s=+3 up to 200 km and for $s=+2$ above 95 km, and show that their amplitudes are almost invariant between 80 and 100 km. Above 106 km, Q2DW amplitudes and phases present structures that might result from the superposition of Q2DWs and their aliased secondary waves.

Quasi-2-day wave in low-latitude atmospheric winds as viewed from the ground and space during January-March, 2020

Maosheng He[1], Jorge L. Chau[1], Jeffrey M. Forbes[2], Xiaoli Zhang[2], Christoph R. Englert[3], Brian J. Harding[4], Thomas J. Immel[4], Lourivaldo M. Lima[5], S. Vijaya Bhaskar Rao[6], M. Venkat Ratnam[7], Guozhu Li[8,9], John M. Harlander[10], Kenneth D. Marr[3], Jonathan J. Makela[11]

[1]Leibniz-Institute of Atmospheric Physics at the Rostock University, Kühlungsborn, Germany.
[2]Ann & H.J. Smead Department of Aerospace Engineering Sciences, University of Colorado, Boulder, USA.
[3]U.S. Naval Research Laboratory, Washington, DC.
[4]Space Sciences Laboratory, University of California Berkeley, Berkeley, CA.
[5]Universidade Estadual da Paraíba, Brazil.
[6]Department of Physics, Sri Venkateswara University, Tirupati, India.
[7]National Atmospheric Research Laboratory, Tirupati, India.
[8]Beijing national observatory of space environment, Institute of Geology and Geophysics, Chinese Academy of Sciences, Beijing, China.
[9]College of Earth and Planetary Sciences, University of Chinese Academy of Sciences, Beijing, China.
[10]Space Systems Research Corporation, Alexandria, VA.
[11]Department of Electrical and Computer Engineering, University of Illinois at Urbana-Champaign, Urbana, IL.

Key Points:

- Q2DW wind field at 80-200 km altitude is delineated from ground and space in the low-latitude region (±15°)
- Zonal wavenumber components $s = +2$ and $s = +3$ are the dominant ones in our observations, and their wave periods evolve differently with time.
- The Q2DW+3 exhibits an excellent quantitative agreement between two datasets at 95–100 km, serving as a validation of the ICON-MIGHTI winds.

Corresponding author: Jorge L. Chau, `chau@iap-kborn.de`

Abstract

Horizontal winds from four low-latitude ($\pm 15°$) specular meteor radars (SMRs) and the MIGHTI instrument on the ICON satellite, are combined to investigate quasi-2-day waves (Q2DWs) in early 2020. SMRs cover 80-100 km altitude whereas MIGHTI covers 95-300 km. Q2DWs are the largest dynamical feature of the summertime middle atmosphere. At the overlapping altitudes, comparisons between the derived Q2DWs exhibit excellent agreement. The SMR sensor array analyses show that the dominant zonal wavenumbers are $s = +2$ and $+3$, and help resolve ambiguities in MIGHTI results. We present the first Q2DW depiction for $s = +3$ up to 200 km and for $s = +2$ above 95 km, and show that their amplitudes are almost invariant between 80 and 100 km. Above 106 km, Q2DW amplitudes and phases present structures that might result from the superposition of Q2DWs and their aliased secondary waves.

Plain Language Summary

In the mesosphere and lower-thermosphere, quasi-2-day waves are spectacular planetary-scale oscillations. Almost all relevant observational studies are based on ground-based single-station or single-satellite methods and therefore cannot determine the zonal wavenumber unambiguously. In the current work, we employ a series of multi-station methods on winds measured by four longitudinally separated low-latitude ground-based radars. These methods help us to determine two dominant zonal wavenumbers at 80–100 km altitude. These results are used to complement satellite measurements. The agreement between datasets is extraordinary, allowing us to extend the characteristics of the waves to higher altitudes using satellite measurements.

1 Introduction

Quasi-two-day waves (Q2DWs) in the mesosphere have been the subject of numerous observational and theoretical investigations (e.g., Pancheva et al., 2018, and references therein) since their first discovery in specular meteor radar (SMR) winds (Müller, 1972). Q2DWs are generally thought to be the atmospheric manifestation of the gravest westward-propagating Rossby-gravity normal mode with zonal wavenumber $s = 3$ (Salby & Roper, 1980; Salby, 1981), amplified or perhaps even initiated by the mesospheric eastward jet instability (Randel, 1994; Plumb, 1983; Pfister, 1985), which admits zonal wavenumbers of $s = 2$ through 4. Q2DWs with $s = 2$, 3, and 4 are common features of space-based observational studies (e.g., Lieberman, 1999; Tunbridge et al., 2011; Gu et al., 2013; Huang et al., 2013).

Being the largest dynamical features of the summertime middle atmosphere, Q2DWs play a significant role in atmosphere-ionosphere coupling. Although earlier works have suggested that Q2DWs could drive F-region ionospheric variability (Ito et al., 1986; Chen, 1992; Pancheva, 1988; Pancheva & Lysenko, 1988), it was not until the last decade that a general circulation model (GCM) including ionospheric electrodynamics demonstrated that the Q2DWs could penetrate above 100 km to produce dynamo electric fields that drive Q2DW ionospheric variability in the F-region (Yue, Wang, et al., 2012). However, it is also known that such penetration is highly sensitive to the zonal-mean wind distribution above 100 km, which is poorly specified (Yue, Liu, & Chang, 2012). In addition, there are remaining questions concerning other ways in which Q2DWs transmit their influence to the ionosphere, including the modulation of tides (Yue et al., 2016) and gravity waves (Meyer, 1999). Other relevant aspects of the problem include the latitude and longitude structure of Q2DWs at any given time. Therefore, further study of the spatial-temporal evolution of Q2DWs and their interactions with other waves appears warranted before a complete understanding of atmosphere-ionosphere coupling is attained.

The pros and cons of ground- and space-based measurements of Q2DWs in the mesosphere and lower thermosphere (MLT) are well-known. Single-station ground-based measurements provide excellent temporal resolution but no information on their horizontal wavenumber (e.g., Harris & Vincent, 1993). On the other hand, satellite measurements provide a more global view in terms of spatial coverage, but suffer from crude temporal resolution and, most significantly, aliasing (Tunbridge et al., 2011; Forbes & Moudden, 2012; Nguyen et al., 2016). When viewed from a quasi-Sun-synchronous perspective in space, a wave at frequency f with zonal wavenumber s is Doppler-shifted such that its longitude structure appears at its "space-based zonal wavenumber" $k_s = |s - \frac{f}{1\text{cpd}}|$, where cpd is cycles per day (e.g., Forbes & Moudden, 2012).

Accordingly, the Q2DW+3 (hereafter, Q2DWp denotes a Q2DW with wavenumber $s = p$) appears at $k_s = 2.5$, and so do secondary waves (SWs) of nonlinear interactions between Q2DW+3 and all migrating tides (Tunbridge et al., 2011; Forbes & Moudden, 2012; Nguyen et al., 2016). These SWs are at frequencies near 0.5, 1.5, 2.5, 3.5, ..., cpd, namely, at periods near 2 day, 16 h, 9.6 h, 6.9 h,... (e.g., He et al., 2021). In other words, these waves will alias into each other when observed from quasi-Sun-synchronous single-spacecraft missions. Among these waves is the Q2DW-2, the near-2-day SW from a Q2DW+3 interaction with the migrating diurnal tide. Similarly, Q2DW+2 and Q2DW+4 can alias with Q2DW-1 and Q2DW-3 at $k_s = 2.5$ and 3.5, respectively. Both Q2DW-2 and Q2DW-3 can arise from jet instabilities at middle to high latitudes during local winter (Pancheva et al., 2016), and all three eastward-propagating Q2DWs can coexist at low latitudes in the form of ultra-fast Kelvin waves (UFKW)(e.g., Forbes, He, et al., 2020; Pancheva et al., 2016).

Despite the importance of dynamo-region winds to Q2DW-ionosphere coupling, wind observations are extremely rare above about 105 km. One exception appears to be Ward et al. (1996) who reported Q2DW+3 winds between 90 and 150 km from Wind Imaging Interferometer (WINDII) daytime measurements on the Upper Atmosphere Research Satellite (UARS) during January 1993. Nighttime satellite measurements are unavailable above 105–110 km due to lack of airglow. This exacerbates sampling issues associated with space-based observations. But combining ground and space partially alleviates this ambiguity, as shown in this study.

As suggested by Harris and Vincent (1993), combining more than one ground-based station could enable a determination of Q2DWs wavenumbers. In the present work, we combine horizontal winds from multiple SMRs (MSMR) located at four different longitudes at low latitudes, and from MIGHTI (Michelson Interferometer for Global High-resolution Thermospheric Imaging) on NASA's ICON (Ionospheric CONnection explorer) satellite (Immel et al., 2018). This combination allows us to obtain a comprehensive view of the Q2DWs that occurred during January–March 2020. Combining the MSMR and

MIGHTI analyses, we are able to characterize clearly the dominant Q2DWs in time, altitude, frequency, wavenumber, and latitude.

2 Data analysis

The current work investigates Q2DWs using MLT zonal (u) and meridional (v) winds collected on the ground and from space. Ground-based winds were obtained between 80 and 100 km every hour at four SMRs: Peru (77°W, 12°S), and Cariri (36.5°W, 7.4°S), Tirupati (79.4°E, 13.6°N) and Ledong (109.0°E, 18.4°N). Characteristics and some results of each of these SMRs can be found in Chau et al. (2021), Lima et al. (2012), S. V. B. Rao et al. (2014), and Wang et al. (2019), respectively. The space-based winds are collected by the MIGHTI instrument on ICON (Englert et al., 2017). From a theoretical study, MIGHTI's wind accuracy is better than 5.8 ms^{-1} 80% of the time. The exceptions occur near the day/night boundaries and occasionally near the equatorial ionization anomaly (in the F-region), due to variations of wind and emission rate along the line-of-sight (Harding et al., 2017). Recently, MIGHTI winds in the F-region (red line) and E-region (green line) have been validated against Fabry-Perot interferometers and SMRs, respectively (Makela et al., 2021; Harding et al., 2021). At low latitudes, Q2DWs maximize annually during January and March (e.g., Harris & Vincent, 1993; N. V. Rao et al., 2017), thus, our study is focused on the January–March 2020 period.

2.1 Multi-station specular meteor radar analyses

At a given frequency f, longitude λ, and time t, the superposition of zonal traveling waves, indexed as $l = 1, 2, ..., L$, with zonal wavenumbers s_l, can be denoted as,

$$\sum_{l=1,2,\ldots,L} \tilde{\Psi}(\lambda, t|f, s_l) = e^{i2\pi ft}\tilde{a}_\lambda \qquad (1)$$

where $\tilde{a}_\lambda = \sum \tilde{A}(\lambda|s_l)$ and $\tilde{A}(\lambda|s_l) = \tilde{A}_l e^{is\lambda}$ is the longitude-dependent complex amplitude. We estimate $\tilde{a}_\lambda$ as a function of f, t, and altitude h, through Lomb-Scargle spectral analyses within a 23-day wide sliding window for each of the wind components of each SMR. The resultant $\tilde{a}_\lambda(t, f, h)$ enable estimation of s and $\tilde{A}_l$ using a variety of sensor array analyses.

Assuming a single dominant wave, i.e., $L = 1$, one can apply the phase difference technique to a pair of SMRs (e.g., He et al., 2018). The single-wave assumption is often facilitated through high-frequency-resolved wavelet or Lomb-Scargle analyses by separating waves in the frequency domain (e.g., He et al., 2018). The current work applies this technique to Tirupati-Ledong and Peru-Cariri pairs, separately. These pairs have been selected given their similar latitudes and relative close longitudinal proximity.

The same wind data have also been analyzed, assuming a dominant wave (i.e., $L = 1$) weakly dependent in latitude. In this case, a least-square estimation (LSE) method similar to Equation A3 in He et al. (2020) has been applied to the altitude-averaged Lomb-Scargle estimations $\langle \tilde{a}_\lambda(t, f, h) \rangle$ from all four radars. This analysis allows determining the dominant wavenumbers for a given period and time.

As we will see later in Section 3, the techniques implemented above reveal that the Q2DWs are dominated mainly by two wavenumbers. While the above techniques use the single-wave assumption, these two dominant waves might superpose on each other. To decompose the potential superposition and estimate the wave amplitudes, we implement an LSE to Equation (1) after relaxing the single-wave assumption to a two-wave assumption, i.e., $L = 2$. A similar procedure was applied by He and Chau (2019) but for near-12-h waves. In the results presented below, the amplitudes are set to zeros either when $\langle \tilde{a}_\lambda(t, f, h) \rangle$ are below the significance level $\alpha = 0.01$ at more than two stations or when the coefficient of determination of the LSE is below $r^2 = 0.7$. The significance level is estimated through a Monte Carlo method.

2.2 ICON-MIGHTI winds

As a slowly precessing low-earth-orbit satellite, ICON orbits at 590–607 km altitude about 15 times per day. ICON crosses a given latitude once in the ascending or descending leg which crosses all local solar times once every 46 days, namely, one orbital precession period. Constrained by the 27° orbital inclination and MIGHTI's viewing geometry off the north side of the spacecraft, the winds are derived between 12°S and 42°N latitude. The ascending-descending differences in the local time are latitude-dependent, which increases from near zero at 12°S to almost 12 h near 18°N and then decreases to less than 2 h at 42°N. MIGHTI winds are derived from the Doppler shift of airglow emissions along with two perpendicular tangent-point line-of-sight vector measurements on the limb. Due to the day-night difference of the airglow's vertical distribution, the altitude coverage of the observations is different between day and night. While the nighttime wind is derived from about 94–106 km, the daytime wind is available at least up to 300 km. In this work, we use the green-line winds, which cover up to 200 km (e.g., Harding et al., 2021).

At 96–106 km altitude, we estimate Q2DW amplitudes as a function of time, frequency, latitude and altitude, by fitting data sampled within a 23-day sliding window, irrespective of the local time, to a single wave model $\tilde{A}_0(s)e^{i(2\pi ft+s\lambda)}$, for $s = 2$ and 3, respectively. Above 106 km and for the amplitude fitting, we sample the only-daytime-available data within time intervals when strong Q2DWs are detected below 106 km, e.g., DOY (day of the year) 15–23 and DOY 39–46. As an example of the data distribution within these two intervals, Figure S1 in the supplemental information presents the samplings as a function of time and subdivided longitude (cf, Moudden & Forbes, 2014) at a given latitude and altitude.

3 Results

Under the single-wave assumption, dominant wavenumbers were obtained by (a) using the phase difference technique on SMR pairs, and (b) using LSE on all four SMRs but assuming a weak latitudinal dependence. We found that in both cases the dominant Q2DW wavenumbers were $s = 3$ and $s = 2$, i.e., Q2DW+3, and Q2DW+2, respectively. Furthermore, we find that the meridional component is much stronger than the zonal component for both dominant wavenumbers. The results of these two analyses are presented in the supplemental material Figures S2 and S3, respectively.

Based on these supporting results, we present the results of relaxing the assumption of one dominant wavenumber for a given time, frequency and altitude, to allow two, i.e., $L = 2$. Figure 1 shows the meridional amplitudes as a function of time and period resulting from fitting for $s = 2$ (left) and $s = 3$ (right) at four altitude ranges, i.e., 80-85 km, 85-90 km, 90-95 km, and 95-100 km.

As displayed in Figure 1a(1b), the Q2DW+2(Q2DW+3) amplitude at 95–100 km altitude maximizes within DOY 40–75(10–40) at period 44–48(48–53) h above 15 ms^{-1}(30 ms^{-1}). The period and amplitude variations of Q2DW+2 and Q2DW+3 at 95–100 km altitude are similar to those at the other three altitudes.

MIGHTI winds complement the MSMR results by extending the Q2DW amplitudes to broader latitude and altitude ranges. In the time-latitude structures of the MIGHTI

Q2DWs at 98 km, as shown in Figure 2, the meridional wind (v) amplitudes of both Q2DWs are significantly stronger than the zonal wind (u) amplitudes, consistent with MSMR results in Figure S2. In v, both Q2DWs attain values of order 20–30 ms^{-1} within ±12° latitude and maximize around the equator. The u amplitudes attain values above 10 ms^{-1} which is confined to latitudes poleward of 10°N.

In Figure 3 we present a qualitative and quantitative comparison of the estimated Q2DW amplitudes obtained with MSMR and MIGHTI. In Figures 3a–3d, the time-frequency spectra of the MSMR Q2DW amplitudes at 95–100 km are in a good qualitative agreement with MIGHTI estimates at 98 km. For a quantitative comparison, we sample every pixel in the MIGHTI spectra of Q2DW+2 and Q2DW+3 and scatter them against the corresponding MSMR amplitudes in Figures 3e and 3f, respectively. Overall, the MIGHTI Q2DW+2 is stronger than the MSMR amplitudes. The former attains 20–25 ms^{-1} whereas the latter is below 15 ms^{-1}. In the case of Q2DW+3, MIGHTI results exhibit excellent quantitative agreement with the MSMR results, both of which attain 30 ms^{-1}.

The fitted amplitudes and phases for MIGHTI results above 96 km are shown in Figure 4 as a function of height at 0° and 15°N latitude. The profiles centered on −5°, +5° and +25° are not sufficiently different from neighboring profiles and therefore not shown here. Within DOY 15–23, the amplitudes maximize generally below 140 km where the profiles often possess two peaks. Also, the v maximum is about a factor of two smaller ($\lesssim$10 ms^{-1}) for Q2DW+2 as compared with Q2DW+3 ($\sim$20 ms^{-1}), whereas the u maximum for Q2DW+2 (12–14 ms^{-1}) is slightly larger than that for Q2DW+3. In addition, half the amplitude profiles show increases with altitude above a minimum near 140–150 km altitude, suggesting a source at higher altitudes. The profiles within DOY 41–49 share many of the same characteristics.

4 Discussions

In the low-latitude middle atmosphere, Q2DWs maximize annually during late January and early February (Palo & Avery, 1996; Harris & Vincent, 1993). Harris and Vincent (1993) noted that the Q2DW-like oscillation in January–February 1991 occurs predominantly at a period 48–50 h, associated with a weaker one at 44 h. According to these periods the authors suggested that the oscillations are manifestations of Rossby-gravity modes Q2DW+3 and Q2DW+2, but could not determine s since they used single-station observations. Our multi-station analyses reveal that during January–February 2020 the most dominant Q2DWs are Q2DW+3 at 48–53 h and Q2DW+2 at 44-48 h. In addition, we find that: (a) the maximum Q2DW+3 amplitude is much stronger than the Q2DW+2 maximum, by a factor of about two, and (b) the Q2DW+3 are almost invariant within 80–100 km altitude, although slightly weaker at 80–85 km than at 85–100 km. Our analyses are the first to directly support the wavenumber suggestions of Harris and Vincent (1993).

Note that our MSMR amplitudes are fitted according to the model of two waves with preassigned s which have to be determined prior to the fitting. Therefore, when the spectrum in the time-frequency depiction is dominated by a third s, the estimation cannot be properly fitted. For example, in Figure S3 besides $s = +3$ and +2, the $s = +1$ and +4 dominate also few pixels within DOY 1–60. At these pixels, the amplitudes are not fitted for Q2DW+1 and Q2DW+4 due to constraints of the two-wave model ($r^2 < 0.7$). Besides, these four dominant Q2DWs might interact nonlinearly with diurnal migrating tides, generating SWs of Q2DW-3, Q2DW-2, Q2DW-1, and , Q2DW0. Additional low-latitude SMRs are desirable to resolve the above-mentioned Q2DWs.

In terms of the temporal evolution of Q2DW+3 amplitude and periods, MSMR results at 95–100 km are in excellent qualitative agreement with the MIGHTI results. The agreement reveals that locally Q2DW+3 is dominantly stronger than its potential aliased waves, e.g., Q2DW-2, near-16-h and -9.6-h SWs, and near-2-day UFKW at $s = -2$, as explained in the introduction. Therefore MSMR help to resolve this type of ambiguity in MIGHTI Q2DW results. However, Q2DW+2 are stronger in the MIGHTI winds than in MSMR winds. The discrepancy is possibly attributable to a superposition in the MIGHTI amplitude between Q2DW+2 and its potential aliased waves, e.g., Q2DW–1.

At altitudes not covered by MSMRs, e.g., above 106 km, the aliased and the superposition might also exist. The superposition could produce the vertical double-peak feature below 140 km altitude observed in Figure 4, associated in some cases with discontinuities, which would be unexpected for a vertically-propagating monochromatic wave. The phases often show downward(upward) phase progressions with altitude, indicative of upward(downward) energy propagation. MLT GCM simulations produced near-48-h, -16-h, -9.6-h SWs arising from interactions of Q2DW+3 with diurnal and semidiurnal migrating tides (Palo et al., 1999; Nguyen et al., 2016; Gu et al., 2018). These SWs appear in the simulations as independent, global-scale vertically-propagating oscillations that extend to at least 50°N in January. Moreover, the simulations demonstrate that these SWs are capable of propagating into the 100–140 km region, and in some cases, above 160 km. It is, therefore, reasonable to assume that during Q2DW events, measurable SWs can simultaneously occur over broad latitude-altitude regimes, and that more appropriate designations in the context of space-based observations are "apparent" Q2DW+2, Q2DW+3, and Q2DW+4.

No studies to date have considered the possibility of SW generation in the lower and middle thermosphere (∼100–250 km) where the migrating tidal winds exist due to thermal forcing by extreme ultraviolet solar radiation, and where the vertically-propagating semidiurnal migrating tide maintains large amplitudes (Figure 6 in Forbes, Zhang, & Maute, 2020). Palo et al. (1999) furthermore invoked the Teitelbaum and Vial (1991) formulation of wave-wave interactions to demonstrate that a myriad of wave products can originate from multi-step SW-tide interactions, including the secondary Q2DWs as products, which complicates the aliasing situation. This secondary Q2DW production parallels the secondary production of the thermospheric Q6DW (demonstrated quantitatively in Forbes, Zhang, & Maute, 2020). Our interpretation that these processes are likely active in defining the vertical amplitude and phase structures of Q2DW+3 and Q2DW+2 in Figure 4 warrants further theoretical and modeling attention.

A similar double-peak feature was also observed in the southern hemisphere Q2DW+3 in WINDII v profiles up to 150 km during January 19–31, 1993 (Ward et al., 1996). During this event, Q2DW+3 amplitudes and phases were estimated between 96–102 km and 70°S–40°N using WINDII, between 70–110 km and 60°S–20°N using the High Resolution Doppler Imager (HRDI) on UARS, and between 94–136 km altitude using winds collected by the Arecibo incoherent scatter radar (18°N) (Wu et al., 1993). Furthermore, the UARS analyses assumed $T = 48$ h and $s = 3$.

In terms of Q2DW penetration into the winter hemisphere, the UARS results at 95–100 km are consistent with our Q2DW+3 results in that they (a) reflect an equatorial maximum in v with a monotonic decrease to less than half the maximum value by 30°N, and (b) a minimum in u at the equator and maximum as far north as $30 - 40°$ latitude. However, both the u and v maxima are about a factor of 2 greater during 1993 than during 2020.

From a more global perspective, Ward et al. (1996) noted in their Figure 3 the similarity of the meridional 3-peaked(2-peaked) structure of $u(v)$ between 70°S–40°N with those in the Q2DW+3 simulations of Hagan et al. (1993). Similar features are also seen in Palo et al. (1999) simulations, but the GCM $u(v)$ structures in Yue, Wang, et al. (2012) are more 2-peaked(1-peaked). All of these results maintain an equatorial minimum in u and a monotonic decrease in v poleward of the equator into the Northern Hemisphere. The tendency for an equatorial maximum in v, and maxima in u poleward of the equator is consistent with the attribution of Q2DW+3 as a Rossby-gravity wave. Therefore, the latitude structures of v and u for Q2DW+3 depicted in Figures 2a and 2c at 98 km are broadly consistent with prior observations, theory, and modeling.

Another unique aspect of the current work is the delineation of both Q2DW+3 and Q2DW+2 vertical structures up to 200 km altitude during a period of deep solar minimum, when vertically-propagating waves should penetrate efficiently in the thermosphere (Oberheide et al., 2009; Häusler et al., 2013). Of particular relevance is the degree to which the Q2DW wind field penetrates to altitudes in the vicinity of the peak Hall (∼106 km) and Pedersen (∼ 125 km) conductivities, where electric fields can be generated and subsequently map into the F-region. This vertical penetration is in fact reflected in Figure 4, but it remains to be determined to what extent the amplitudes and vertical phase structures yield sufficiently large field-aligned-integrated conductivity-weighted winds to drive F-region ionospheric variability of any significance.

5 Summary and conclusions

In this work, we combine MLT winds observed by four longitudinally separated low-latitude SMRs and by MIGHTI on the ICON satellite to investigate Q2DWs during January–March 2020. Based on different but complementary sensor array analyses, we identify that Q2DWs are dominated by Q2DW+3 and Q2DW+2, at periods $T = 48-53$ h and 44–48 h, respectively. These are the first observations of such waves and support the suggested Q2DW wavenumbers of Harris and Vincent (1993) based on single-station observations.

Our MSMR Q2DW amplitudes are almost altitude-independent within 80–100 km. Their 95–100 km time-frequency structures compared well with the amplitudes estimated from MIGHTI winds. In the comparison, Q2DW+3 exhibits an excellent quantitative agreement whereas the Q2DW+2 exhibits only a reasonable qualitative agreement with stronger amplitudes in MIGHTI than in MSMR results. Based on this agreement, we are able to resolve the period and wavenumber ambiguity in MIGHTI estimates. We attribute the discrepancy to the existence of aliased waves.

The MIGHTI measurements are further used to assess the degree of latitudinal and vertical penetration of the Q2DWs, up to 42°N and 200 km. At 98 km and for both Q2DW+2 and Q2DW+3, the amplitudes in v are stronger than in u. For Q2DW+3, these features are largely consistent with prior observations, theory and modeling, whereas for Q2DW+2 the height-latitude structures have not appeared in prior observational or modeling studies. Above 106 km, the amplitudes become vertically structured. These vertical structures are attributable to the superposition between Q2DWs and their aliased waves.

Acknowledgments

This work was supported by the Deutsche Forschungsgemeinschaft (DFG, German Research Foundation) under SPP 1788 (DynamicEarth)-CH 1482/1-2 (DYNAMITE). C. Englert, J. Forbes, B. Harding, T. Immel, J. Makela, J. Harlander, K. Marr, and X. Zhang gratefully acknowledge support for this project by the ICON mission, which is supported by NASA's Explorers Program through contracts NNG12FA45C and NNG12FA42I. G. Li acknowledges the support of NSFC (42020104002, 41727803).

Open Research Data Statement

The hourly wind data from Ledong is provided by the Data Center for Geophysics, National Earth System Science Data Sharing Infrastructure at BNOSE, IGGCAS (`http://wdc.geophys.ac.cn/`). The post-processed MSMR data used in the current paper are available at DOI 10.22000/421 (`https://www.radar-service.eu/radar/en/dataset/sHWduLXVNoaZNhUQ?token=ZVxakQZEdrDaNMpWpgtF`). The ICON-MIGHTI winds are publicly available at the ICON data center (https://ICON/MIGHTI.ssl.berkeley.edu/Data).

References

Chau, J. L., Urco, J. M., Vierinen, J., Harding, B. J., Clahsen, M., Pfeffer, N., ... Erickson, P. J. (2021). Multistatic Specular Meteor Radar Network in Peru: System Description and Initial Results. *Earth Sp. Sci.*, *8*(1), e2020EA001293. doi: 10.1029/2020EA001293

Chen, P.-R. (1992). Two-day oscillation of the equatorial ionization anomaly. *J. Geophys. Res.*, *97*(A5), 6343. doi: 10.1029/91ja02445

Englert, C. R., Harlander, J. M., Brown, C. M., Marr, K. D., Miller, I. J., Stump, J. E., ... Immel, T. J. (2017). Michelson Interferometer for Global High-Resolution Thermospheric Imaging (MIGHTI): Instrument Design and Calibration. *Space Sci. Rev.*, *212*(1-2), 553–584. Retrieved from `https://doi.org/10.1007/s11214-017-0358-4` doi: 10.1007/s11214-017-0358-4

Forbes, J. M., He, M., Maute, A., & Zhang, X. (2020). Ultrafast Kelvin Wave Variations in the Surface Magnetic Field. *J. Geophys. Res. Sp. Phys.*, *125*(9), e2020JA028488. Retrieved from `https://doi.org/10.1029/2020JA028488` doi: 10.1029/2020JA028488

Forbes, J. M., & Moudden, Y. (2012). Quasi-two-day wave-tide interactions as revealed in satellite observations. *J. Geophys. Res. Atmos.*, *117*(12). Retrieved from `https://doi.org/10.1029/2011JD017114` doi: 10.1029/2011JD017114

Forbes, J. M., Zhang, X., & Maute, A. (2020). Planetary Wave (PW) Generation in the Thermosphere Driven by the PW-Modulated Tidal Spectrum. *J. Geophys. Res. Sp. Phys.*, *125*(5), 1–19. doi: 10.1029/2019JA027704

Gu, S. Y., Li, T., Dou, X., Wu, Q., Mlynczak, M. G., & Russell, J. M. (2013). Observations of Quasi-Two-Day wave by TIMED/SABER and TIMED/TIDI. *J. Geophys. Res. Atmos.*, *118*(4), 1624–1639. doi: 10.1002/jgrd.50191

Gu, S. Y., Liu, H. L., Dou, X., & Jia, M. (2018). Ionospheric Variability Due to Tides and Quasi-Two Day Wave Interactions. *J. Geophys. Res. Sp. Phys.*, *123*(2), 1554–1565. doi: 10.1002/2017JA025105

Hagan, M. E., Forbes, J. M., & Vial, F. (1993). Numerical investigation of the propagation of the quasi-two-day wave into the lower thermosphere. *J. Geophys. Res.*, *98*(D12), 23193. doi: 10.1029/93jd02779

Harding, B. J., Chau, J. L., He, M., Englert, C. R., Harlander, J. M., Marr, K. D., ... Immel, T. J. (2021). Validation of ICON-MIGHTI thermospheric wind observations: 2. Green-line comparisons to specular meteor radars. *J. Geophys. Res. Sp. Phys.*, e2020JA028947. doi: https://doi.org/10.1029/2020JA028947

Harding, B. J., Makela, J. J., Englert, C. R., Marr, K. D., Harlander, J. M., England, S. L., & Immel, T. J. (2017). The MIGHTI Wind Retrieval Algorithm: Description and Verification. *Space Sci. Rev.*, *212*(1-2), 585–600.

Retrieved from https://doi.org/10.1007/s11214-017-0359-3 doi: 10.1007/s11214-017-0359-3

Harris, T. J., & Vincent, R. A. (1993). The quasi-two-day wave observed in the equatorial middle atmosphere. *J. Geophys. Res.*, *98*(D6), 10481. doi: 10.1029/93jd00380

Häusler, K., Oberheide, J., Lühr, H., & Koppmann, R. (2013). The geospace response to nonmigrating tides. In *Clim. weather sun-earth syst.* (pp. 481–506). Springer.

He, M., & Chau, J. L. (2019). Mesospheric semidiurnal tides and near-12 h waves through jointly analyzing observations of five specular meteor radars from three longitudinal sectors at boreal midlatitudes. *Atmos. Chem. Phys.*, *19*(9), 5993–6006. Retrieved from https://doi.org/10.5194/acp-19-5993-2019 doi: 10.5194/acp-19-5993-2019

He, M., Chau, J. L., Stober, G., Li, G., Ning, B., & Hoffmann, P. (2018). Relations Between Semidiurnal Tidal Variants Through Diagnosing the Zonal Wavenumber Using a Phase Differencing Technique Based on Two Ground-Based Detectors. *J. Geophys. Res. Atmos.*, *123*(8), 4015–4026. Retrieved from https://doi.org/10.1002/2018JD028400 doi: 10.1002/2018JD028400

He, M., Forbes, J. M., Chau, J. L., Li, G., Wan, W., & Korotyshkin, D. V. (2020). High-Order Solar Migrating Tides Quench at SSW Onsets. *Geophys. Res. Lett.*, *47*(6), 1–8. Retrieved from https://doi.org/10.1029/2019GL086778 doi: 10.1029/2019GL086778

He, M., Forbes, J. M., Li, G., Jacobi, C., & Hoffmann, P. (2021). Mesospheric Q2DW interactions with four migrating tides at 53N latitude: zonal wavenumber identification through dual-station approaches. *Geophys. Res. Lett.*, *48*, e2020GL092237. Retrieved from https://doi.org/10.1029/2020GL092237 doi: 10.1029/2020GL092237

Huang, Y. Y., Zhang, S. D., Yi, F., Huang, C. M., Huang, K. M., Gan, Q., & Gong, Y. (2013). Global climatological variability of quasi-two-day waves revealed by TIMED/SABER observations. *Ann. Geophys.*, *31*(6), 1061–1075. Retrieved from https://angeo.copernicus.org/articles/31/1061/2013/ doi: 10.5194/angeo-31-1061-2013

Immel, T. J., England, S. L., Mende, S. B., Heelis, R. A., Englert, C. R., Edelstein, J., ... Sirk, M. M. (2018). The Ionospheric Connection Explorer Mission: Mission Goals and Design. *Space Sci. Rev.*, *214*(1). Retrieved from `https://doi.org/10.1007/s11214-017-0449-2` doi: 10.1007/s11214-017-0449-2

Ito, R., Kato, S., & Tsuda, T. (1986). Consideration of an ionospheric wind dynamo driven by a planetary wave with a two-day period. *J. Atmos. Terr. Phys.*, *48*(1), 1–13. doi: 10.1016/0021-9169(86)90108-X

Lieberman, R. S. (1999). Eliassen-Palm Fluxes of the 2-Day Wave. *J. Atmos. Sci.*, *56*(16), 2846–2861. doi: 10.1175/1520-0469(1999)056⟨2846:EPFOTD⟩2.0.CO;2

Lima, L. M., Alves, E. O., Batista, P. P., Clemesha, B. R., Medeiros, A. F., & Buriti, R. A. (2012). Sudden stratospheric warming effects on the mesospheric tides and 2-day wave dynamics at 7°S. *J. Atmos. Solar-Terrestrial Phys.*, *78-79*, 99–107. Retrieved from `http://dx.doi.org/10.1016/j.jastp.2011.02.013` doi: 10.1016/j.jastp.2011.02.013

Makela, J. J., Baughman, M., Navarro, L. A., Harding, B. J., Englert, C. R., Harlander, J. M., ... Immel, T. J. (2021). Validation of ICON-MIGHTI Thermospheric Wind Observations: 1. Nighttime Red-Line Ground-Based Fabry-Perot Interferometers. *J. Geophys. Res. Sp. Phys.*, *126*(2), 1–13. doi: 10.1029/2020ja028726

Meyer, C. K. (1999). Gravity wave interactions with mesospheric planetary waves: A mechanism for penetration into the thermosphere-ionosphere system. *J. Geophys. Res. Sp. Phys.*, *104*(A12), 28181–28196. Retrieved from `https://doi.org/10.1029/1999ja900346` doi: 10.1029/1999ja900346

Moudden, Y., & Forbes, J. M. (2014). Quasi-two-day wave structure, interannual variability, and tidal interactions during the 2002–2011 decade. *J. Geophys. Res.*, *119*(5), 2241–2260. doi: 10.1002/2013JD020563

Müller, H. G. (1972). A discussion on D and E region winds over Europe-Long-period meteor wind oscillations. *Philos. Trans. R. Soc. London. Ser. A, Math. Phys. Sci.*, *271*(1217), 585–599. Retrieved from `https://royalsocietypublishing.org/doi/abs/10.1098/rsta.1972.0026` doi: 10.1098/rsta.1972.0026

Nguyen, V. A., Palo, S. E., Lieberman, R. S., Forbes, J. M., Ortland, D. A., & Siskind, D. E. (2016). Generation of secondary waves arising from nonlinear interaction between the quasi 2 day wave and the migrating diurnal tide. *J. Geophys. Res. Atmos.*, *121*(13), 7762–7780. Retrieved from `http://doi.wiley.com/10.1002/2016JD024794` doi: 10.1002/2016JD024794

Oberheide, J., Forbes, J. M., Häusler, K., Wu, Q., & Bruinsma, S. L. (2009). Tropospheric tides from 80 to 400 km: Propagation, interannual variability, and solar cycle effects. *J. Geophys. Res. Atmos.*, *114*(23), 1–18. doi: 10.1029/2009JD012388

Palo, S. E., & Avery, S. K. (1996). Observations of the quasi-two-day wave in the middle and lower atmosphere over Christmas Island. *J. Geophys. Res. Atmos.*, *101*(D8), 12833–12846. Retrieved from `https://agupubs.onlinelibrary.wiley.com/doi/abs/10.1029/96JD00699` doi: https://doi.org/10.1029/96JD00699

Palo, S. E., Roble, R. G., & Hagan, M. E. (1999). Middle atmosphere effects of the quasi-two-day wave determined from a General Circulation Model. *Earth, Planets Sp.*, *51*(7-8), 629–647. Retrieved from `https://doi.org/10.1186/BF03353221` doi: 10.1186/BF03353221

Pancheva, D. (1988). Travelling quasi-two-day fluctuations in the summer F-region. *C. R. Acad. Bulg. Sci.*, *41*(11), 41–44.

Pancheva, D., & Lysenko, I. (1988). Quasi-2-day fluctuations observed in the summer F region electron maximum. *Bulg. Geophys. J.*, *14*(2), 41–51.

Pancheva, D., Mukhtarov, P., & Siskind, D. E. (2018). Climatology of the quasi-2-day waves observed in the MLS/Aura measurements (2005–2014). *J. Atmos. Solar-Terrestrial Phys.*, *171*(April 2017), 210–224. Retrieved from `https://doi.org/10.1016/j.jastp.2017.05.002` doi: 10.1016/j.jastp.2017.05.002

Pancheva, D., Mukhtarov, P., Siskind, D. E., & Smith, A. K. (2016). Global distribution and variability of quasi 2 day waves based on the NOGAPS-ALPHA reanalysis model. *J. Geophys. Res. Sp. Phys.*, *121*(11), 11,422–11,449. doi: 10.1002/2016JA023381

Pfister, L. (1985). Baroclinic instability of easterly jets with applications to the summer mesosphere. *J. Atmos. Sci.*, *42*(4), 313–330. doi: 10.1175/1520-0469(1985)042⟨0313:BIOEJW⟩2.0.CO;2

Plumb, R. A. (1983). Baroclinic instability of the summer mesosphere: a mechanism for the quasi-two-day wave? *J. Atmos. Sci.*, *40*(1), 262–270. doi: 10.1175/1520

-0469(1983)040⟨0262:BIOTSM⟩2.0.CO;2

Randel, W. J. (1994). Observations of the 2-day wave in NMC stratospheric analyses. *J. Atmos. Sci.*, *51*(2), 306–313. doi: 10.1175/1520-0469(1994)051⟨0306:OOTDWI⟩2.0.CO;2

Rao, N. V., Ratnam, M. V., Vedavathi, C., Tsuda, T., Murthy, B. V. K., Sathishkumar, S., … Rao, S. V. B. (2017). Seasonal, inter-annual and solar cycle variability of the quasi two day wave in the low-latitude mesosphere and lower thermosphere. *J. Atmos. Solar-Terrestrial Phys.*, *152-153*, 20–29. Retrieved from `https://www.sciencedirect.com/science/article/pii/S1364682616304084` doi: https://doi.org/10.1016/j.jastp.2016.11.005

Rao, S. V. B., Eswaraiah, S., Venkat Ratnam, M., Kosalendra, E., Kishore Kumar, K., Sathish Kumar, S., … Gurubaran, S. (2014). Advanced meteor radar installed at Tirupati: System details and comparison with different radars. *J. Geophys. Res.*, *119*(21), 11,893–11,904. doi: 10.1002/2014JD021781

Salby, M. L. (1981). Rossby normal modes in nonuniform background configurations. Part II: Equinox and solstice conditions. *J. Atmos. Sci.*, *38*(9), 1827–1840. doi: 10.1175/1520-0469(1981)038⟨1827:RNMINB⟩2.0.CO;2

Salby, M. L., & Roper, R. G. (1980). Long-Period Oscillations in the Meteor Region. *J. Atmos. Sci.*, *37*(1), 237–244. doi: 10.1175/1520-0469(1980)037⟨0237:lpoitm⟩2.0.co;2

Teitelbaum, H., & Vial, F. (1991). On tidal variability induced by nonlinear interaction with planetary waves. *J. Geophys. Res. Sp. Phys.*, *96*(A8), 14169–14178. Retrieved from `http://doi.wiley.com/10.1029/91JA01019` doi: 10.1029/91ja01019

Tunbridge, V. M., Sandford, D. J., & Mitchell, N. J. (2011). Zonal wave numbers of the summertime 2 day planetary wave observed in the mesosphere by EOS Aura Microwave Limb Sounder. *J. Geophys. Res. Atmos.*, *116*(11), 1–16. doi: 10.1029/2010JD014567

Wang, Y., Li, G., Ning, B., Yang, S., Sun, W., & Yu, Y. (2019). All-Sky Interferometric Meteor Radar Observations of Zonal Structure and Drifts of Low-Latitude Ionospheric E Region Irregularities. *Earth Sp. Sci.*, *6*(12), 2653–2662. doi: 10.1029/2019EA000884

Ward, W. E., Wang, D. Y., Solheim, B. H., & Shepherd, G. G. (1996). Observations of the two-day wave in WINDII data during January, 1993. *Geophys. Res. Lett.*, *23*(21), 2923–2926. doi: 10.1029/96GL02897

Wu, D. L., Hays, P. B., Skinner, W. R., Marshall, A. R., Burrage, M. D., Lieberman, R. S., & Ortland, D. A. (1993). Observations of the quasi 2-day wave from the High Resolution Doppler Imager on Uars. *Geophys. Res. Lett.*, *20*(24), 2853–2856. Retrieved from `https://doi.org/10.1029/93gl03008` doi: 10.1029/93GL03008

Yue, J., Liu, H. L., & Chang, L. C. (2012, mar). Numerical investigation of the quasi 2 day wave in the mesosphere and lower thermosphere. *J. Geophys. Res. Atmos.*, *117*(5). doi: 10.1029/2011JD016574

Yue, J., Wang, W., Richmond, A. D., & Liu, H. L. (2012). Quasi-two-day wave coupling of the mesosphere and lower thermosphere-ionosphere in the TIME-GCM: Two-day oscillations in the ionosphere. *J. Geophys. Res. Sp. Phys.*, *117*(7). doi: 10.1029/2012JA017815

Yue, J., Wang, W., Ruan, H., Chang, L. C., & Lei, J. (2016). Impact of the interaction between the quasi-2 day wave and tides on the ionosphere and thermosphere. *J. Geophys. Res. A Sp. Phys.*, *121*(4), 3555–3563. doi: 10.1002/2016JA022444

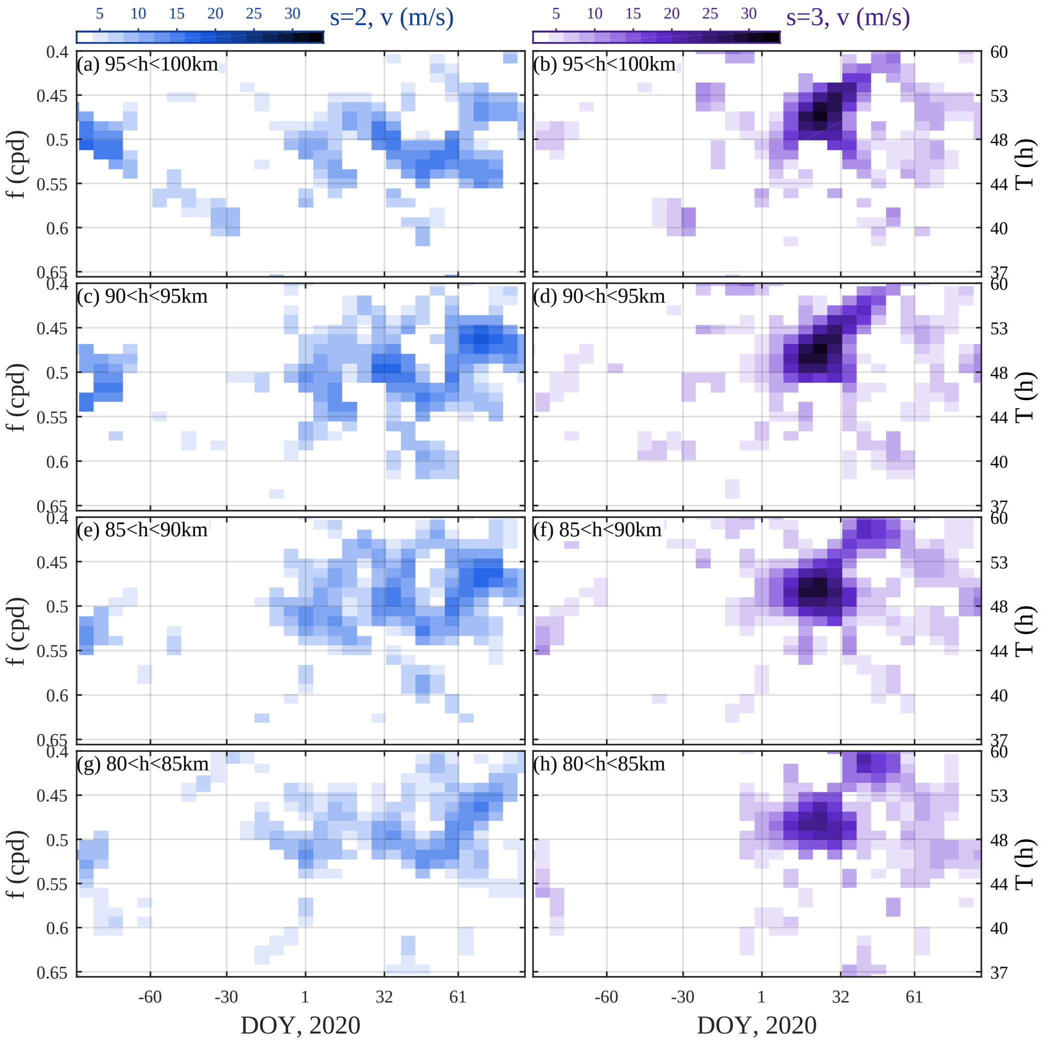

Figure 1: Amplitudes of (blue) Q2DW+2 and (purple) Q2DW+3 in time-frequency depiction, in four altitude ranges estimated using the meridional winds from the four low-latitude radars.

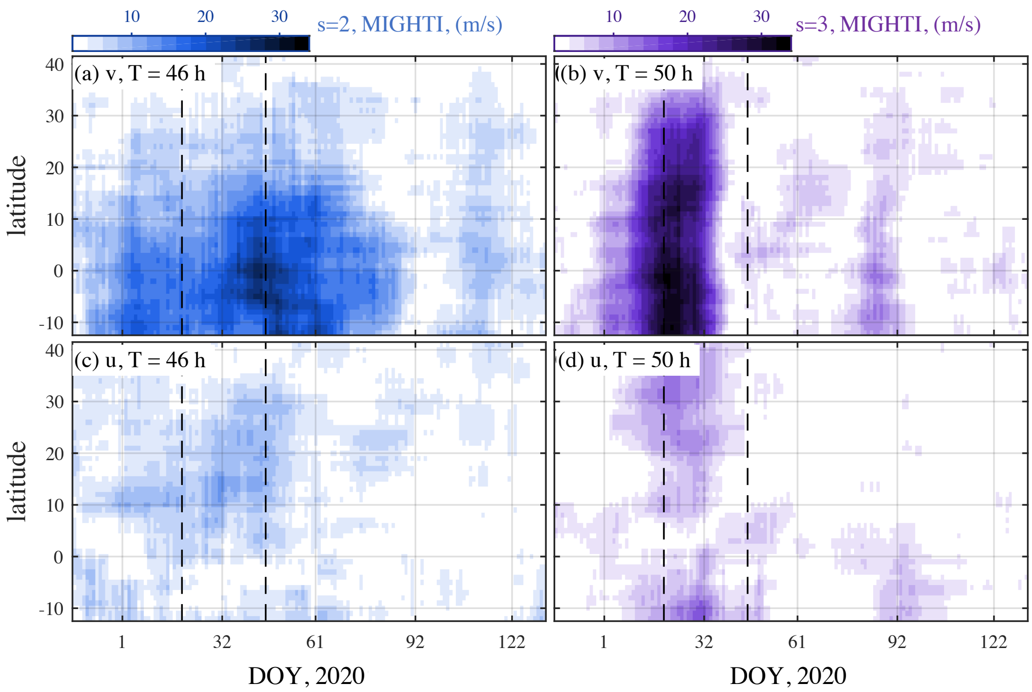

Figure 2: (a) Q2DW+2 amplitude at 46 h period at 98 km altitude in time-latitude depiction estimated from MIGHTI meridional wind. (b) same as (a) but for Q2DW+3 at 50 h period. (c,d) same as (a,b) but estimated from zonal winds. Vertical dashed lines indicate the centers of two 9-day windows used in Figure 4, which contain the maxima of the amplitudes and where daytime wind data are available above 106 km.

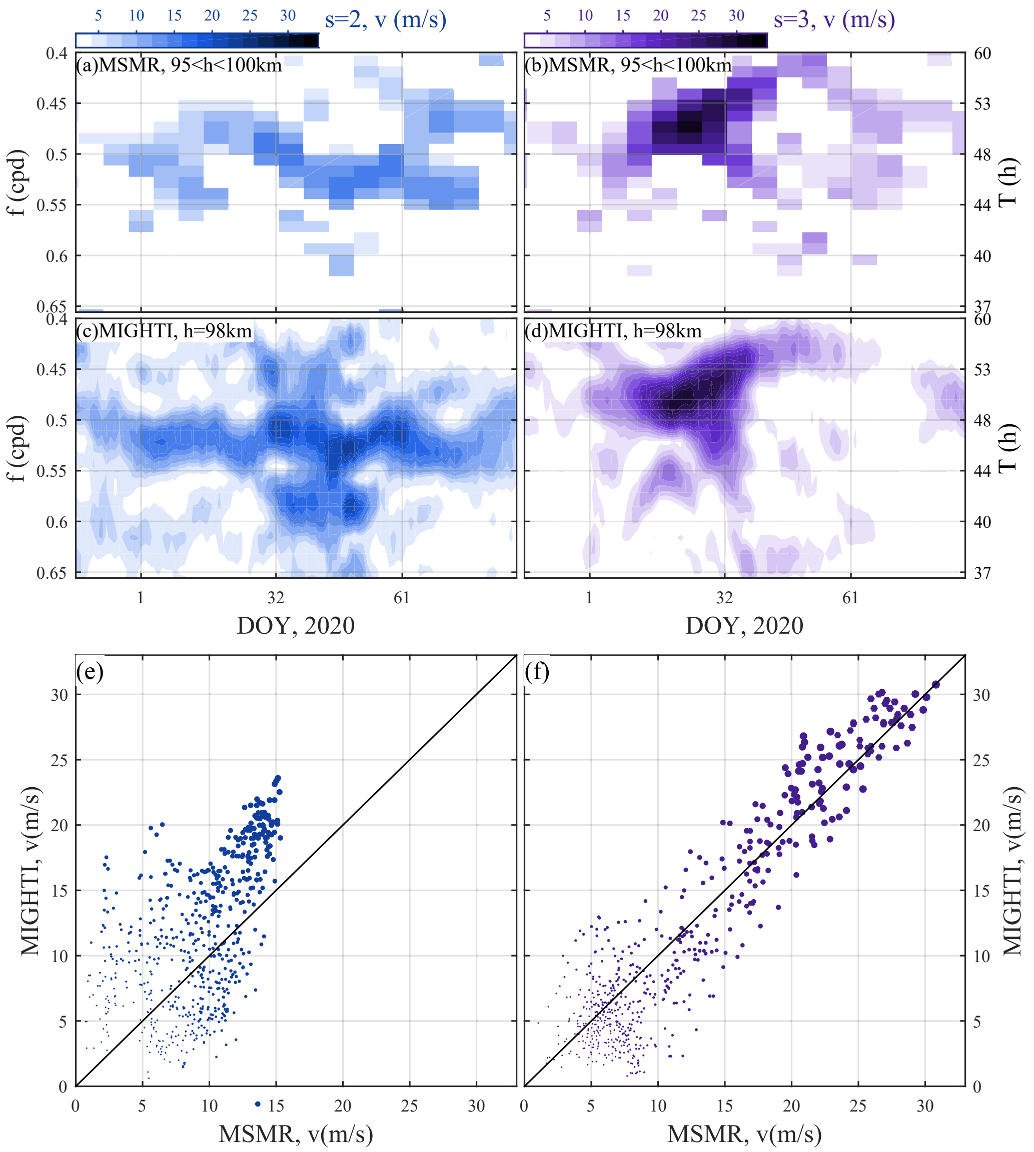

Figure 3: Meridional wind Q2DW+2 and Q2DW+3 amplitude comparisons between MSMR and MIGHTI results. (a, b) MSMR results between 95–100 km for $s = 2$ and $s = 3$, and (c, d) same plots as (a, b) but estimated from MIGHTI winds at 98 km altitude. (e) scatter plot of the values sampled from (a) and (c), in which each point denotes one pixel in (c) and its size is weighted by the sum of the amplitudes' squared. (f) same plots as (e) but sampled from (b) and (d).

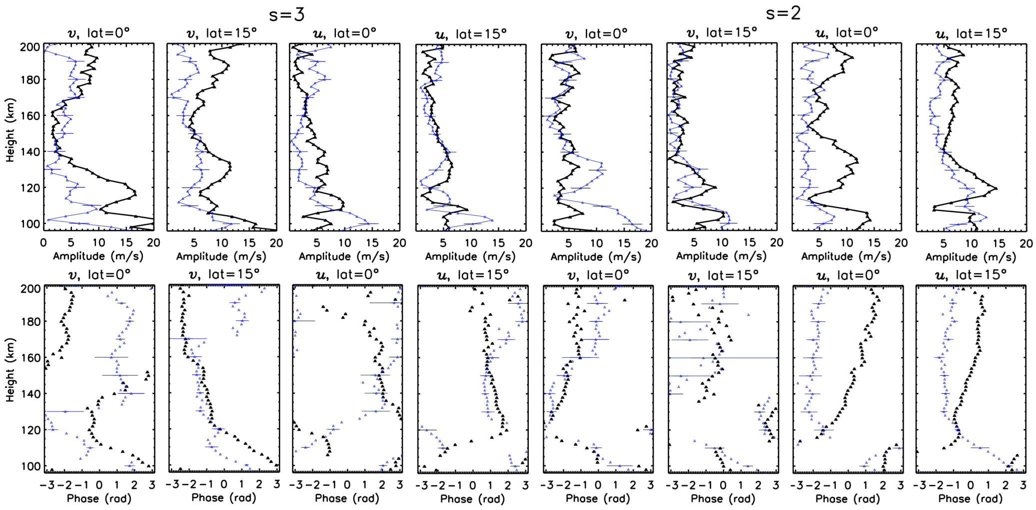

Figure 4: Vertical profiles of amplitude (top) and phase (bottom) u and v centered on latitudes 0° and 15° for Q2DW+3 (left four columns) and Q2DW+2 (right four columns) for DOY 15–23 (black) and DOY 41–49 (blue).

Supporting Information for "Quasi-2-day wave in low-latitude atmospheric winds as viewed from the ground and space during January-March, 2020"

Maosheng He[1], Jorge L. Chau[1], Jeffrey M. Forbes[2], Xiaoli Zhang[2], Christoph R. Englert[3], Brian J. Harding[4], Thomas J. Immel[4], Lourivaldo M. Lima[5], S. Vijaya Bhaskar Rao[6], M. Venkat Ratnam[7], Guozhu Li[8,9], John M. Harlander[10], Kenneth D. Marr[3], Jonathan J. Makela[11]

[1]Leibniz-Institute of Atmospheric Physics at the Rostock University, Kühlungsborn, Germany.

[2]Ann & H.J. Smead Department of Aerospace Engineering Sciences, University of Colorado, Boulder, USA.

[3]Space Science Division, Naval Research Laboratory, Washington, DC.

[4]Space Sciences Laboratory, University of California Berkeley, Berkeley, CA.

[5]Universidade Estadual da Paraíba, Brazil.

[6]Department of Physics, Sri Venkateswara University, Tirupati, India.

[7]National Atmospheric Research Laboratory, Tirupati, India.

[8]Beijing national observatory of space environment, Institute of Geology and Geophysics, Chinese Academy of Sciences, Beijing, China.

[9]College of Earth and Planetary Sciences, University of Chinese Academy of Sciences, Beijing, China.

[10]Space Systems Research Corporation, Alexandria, VA.

[11]Department of Electrical and Computer Engineering, University of Illinois at Urbana-Champaign, Urbana, IL.

Contents of this file

1. Figures S1 to S3

Additional Supporting Information (Files uploaded separately)

1. Captions for Figures S1 to S3

Introduction

The current supporting information comprises three figures.

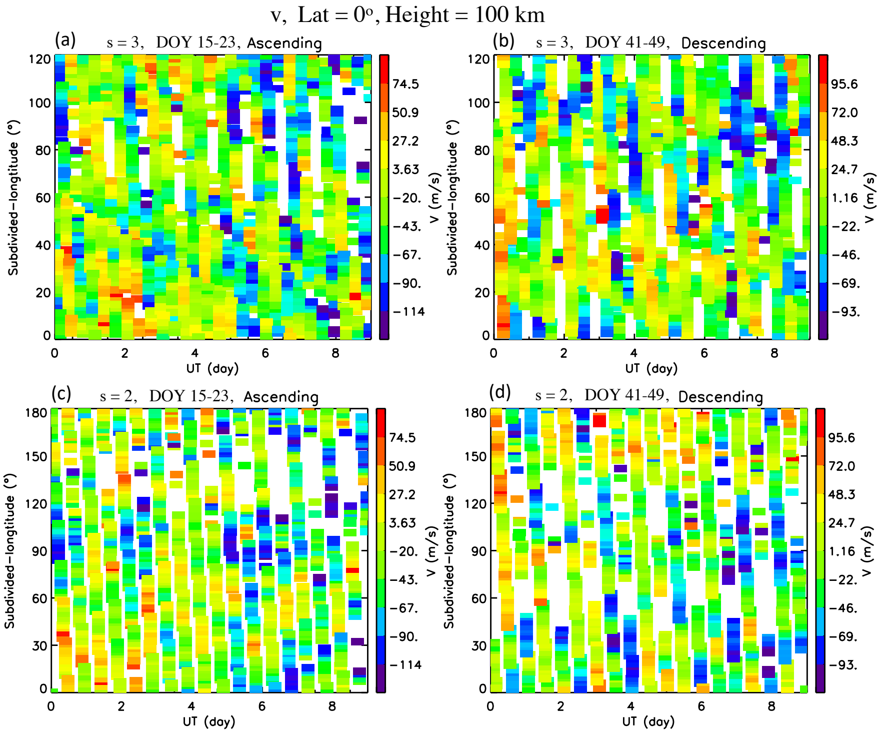

Figure S1. MIGHTI meridional wind at 100 km altitude between 5°S–5°N as a function of subdivided longitude and time for estimating the Q2DW+3 amplitude during DoY (a) 15–23 and (b) 41–49 collected on the ascending and descending legs. (c,d) same plots as (a,b) but for the Q2DW+2 amplitude estimation. Outliers outside ±100 ms^{-1} of the median value have been removed. The sampling distributions here are broadly representative of all the fits that were performed, although the details differ slightly between all latitudes and altitudes and sampling intervals. The subdivided longitude was defined so that $\lambda'(s) := \lambda - 2\pi N_s/s$, $N_s \in \{0, 1, ..., s-1\}$, and $0 < \lambda'(s) < 2\pi/s$, (cf, "longitude subdivision method", LSM, in Moudden & Forbes, 2014). The LSM provides an adequate representation for inspecting the data coverage. At a given latitude, ICON's ascending or descending leg crosses a given longitudinal sector λ once per day and crosses the $\lambda'(s)$ sectors s times per day or $\frac{sT}{1\text{day}}$ times per wave period T (i.e., 6 and 4 times per 48hr for Q2DW+3 and Q2DW+2 as demonstrated in (a, b) and (c, d), respectively).

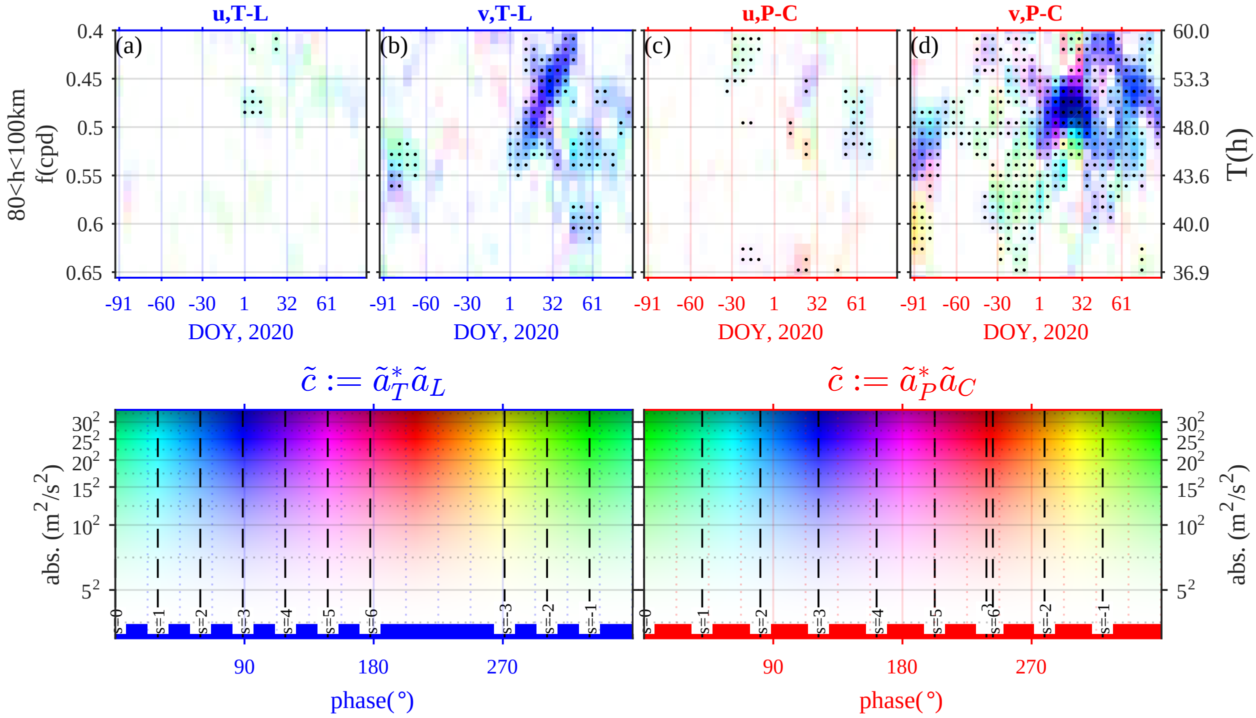

Figure S2. (a) Altitude-averaged (80–100 km) cross product between the 23-day sliding Lomb-Scargle spectrum of the zonal wind collected by the radar at Tirupati and that at Ledong . (b) Same as (a) but for the meridional wind. (c,d) same as (a,b) but between at the Peru-Cariri radar pair. In each panel, the darkness denotes the magnitude; the color hue denotes the longitudinal phase difference which enables determining the zonal wavenumber refers to the color map; and the black dots indicate spectra above the $\alpha = 0.01$ significance level (for details cf, He et al., 2018; He, Chau, et al., 2020). The color bar for each pair are indicated in the bottom row.

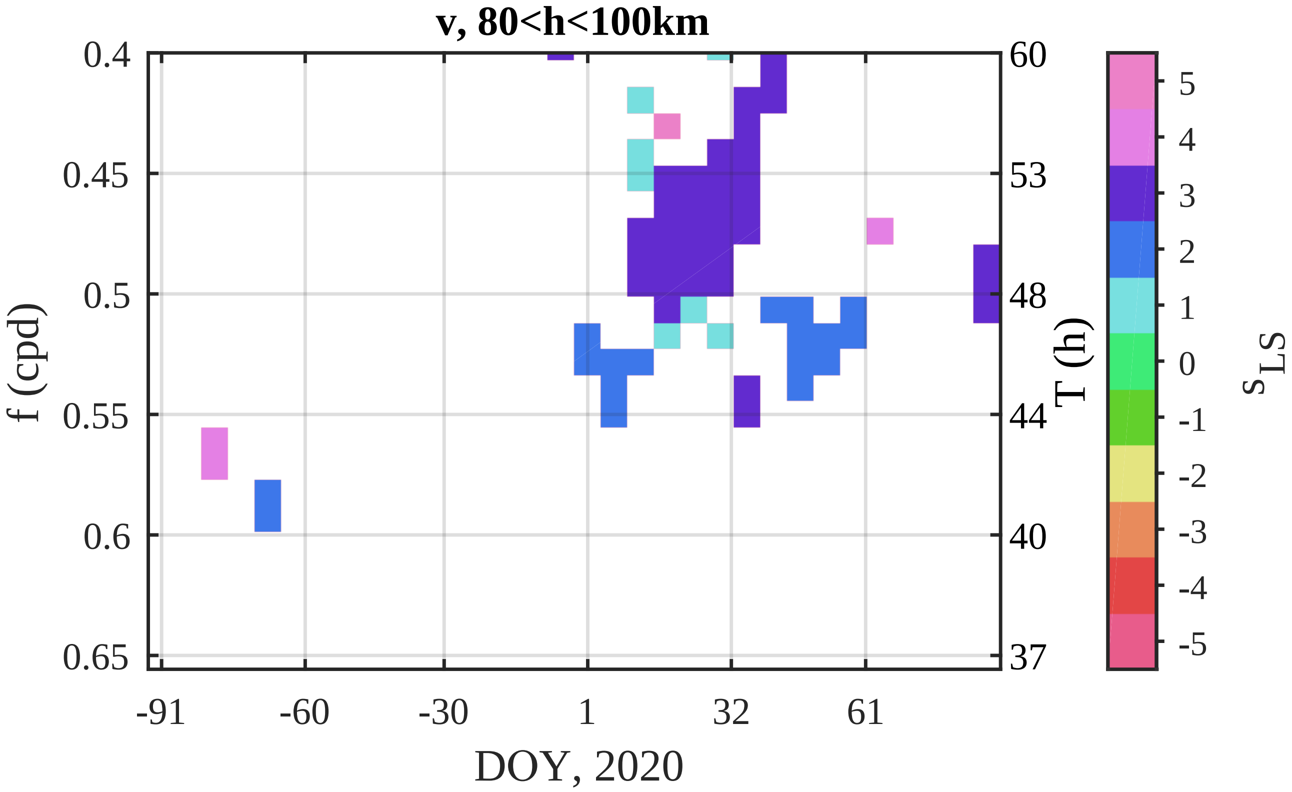

Figure S3. The dominant zonal wavenumber at 80–100km altitude estimated using the meridional winds from all four stations through the least square method $\hat{s}_{LS} = \text{argmin}_{s\in\{-5,-4,\ldots,5\}} \sum_k |\tilde{a}_k - \tilde{A}_0(s)e^{is\lambda_k}|^2$ (see Equation A3 He, Forbes, et al., 2020, for details). Here, $\hat{s}_{LS}$ is displayed only when the least-square coefficient of determination $r^2 > 0.7$ and the Lomb-Scargle spectra $\tilde{a}_k$ are above the significance level $\alpha = 0.01$ at all four stations.

References

He, M., Chau, J. L., Forbes, J. M., Thorsen, D., Li, G., Siddiqui, T. A., ... Hocking, W. K. (2020). Quasi-10-Day Wave and Semidiurnal Tide Nonlinear Interactions During the Southern Hemispheric SSW 2019 Observed in the Northern Hemispheric Mesosphere. *Geophys. Res. Lett.*, *47*(23), e2020GL091453. Retrieved from https://doi.org/10.1029/2020GL091453 doi: https://doi.org/10.1029/2020GL091453

He, M., Chau, J. L., Stober, G., Li, G., Ning, B., & Hoffmann, P. (2018). Relations Between Semidiurnal Tidal Variants Through Diagnosing the Zonal Wavenumber Using a Phase Differencing Technique Based on Two Ground-Based Detectors. *J. Geophys. Res. Atmos.*, *123*(8), 4015–4026. Retrieved from https://doi.org/10.1002/2018JD028400 doi: 10.1002/2018JD028400

He, M., Forbes, J. M., Chau, J. L., Li, G., Wan, W., & Korotyshkin, D. V. (2020). High-Order Solar Migrating Tides Quench at SSW Onsets. *Geophys. Res. Lett.*, *47*(6), 1–8. Retrieved from https://doi.org/10.1029/2019GL086778 doi: 10.1029/2019GL086778

Moudden, Y., & Forbes, J. M. (2014). Quasi-two-day wave structure, interannual variability, and tidal interactions during the 2002–2011 decade. *J. Geophys. Res.*, *119*(5), 2241–2260. doi: 10.1002/2013JD020563